Journal of Materials Science: Materials in Electronics (2020) 31:12089–12100
https://doi.org/10.1007/s10854-020-03754-4

Modified polymer optical fiber sensors for crude oil refractive index monitoring

Zahra Samavati[1] · Alireza Samavati[1] · Ahmad Fauzi Ismail[1] · Noorhana Yahya[2] · Mohd Hafiz Dzarfan Othman[1] · Mukhlis A. Rahman[1]

Received: 18 February 2020 / Accepted: 7 June 2020 / Published online: 13 June 2020

Abstract

The oil concentration as a petroleum quality parameter is an eternal mystery that determines the oil value. We report detection of crude oil refractive index (RI) changes by modified polymer optical fiber (POF) sensor which is prepared via removing the majority of cladding part until ~ 100 nm thickness remains followed by the deposition of discontinuous silver (Ag) nanofilm as an inner layer (~ 20 nm thicknesses) and coating with different shapes of zinc oxide (ZnO) nanostructures including nanoparticles and horizontally and vertically oriented nanorods as an outer layer. Upon conversion from ZnO nanoparticles to vertically oriented ZnO nanorods, the rms roughness, optical band gap, and light transmittance are varied from ~ 23 to ~ 346 nm, ~ 3.45 to ~ 3.20 eV, and 31 to 27%, respectively. The higher sensing performance is obtained for the probe coated with vertically aligned ZnO nanorods at near-infrared wavelength and the value for intensity and wavelength sensitivity are 38 dB/RIU and 78 nm/RIU, respectively. This superior performance is originated from deep penetration of evanescent wave, high surface volume ratio, good crystallinity, adhesive interaction with crude oil molecules, large surface roughness, and high-order dispersion.

1 Introduction

Sensing the RI as a distinctive feature of material plays a predominant role in petroleum industry [1], biochemical analysis [2], agricultural industry [3], environment pollution monitoring [4] and so on. Optical fiber RI sensors are attractive to use in a variety of applications due to immunity to electromagnetic interference, compact size, and remote sensing ability. Recently, RI sensors based on tilted fiber Bragg gratings [5], long period fiber gratings [6], and multimode interference [7, 8] are fabricated using glass optical fiber. POF sensors are commercial promising device for liquid RI detection due to greater flexibility, easier handling, operation in visible region and, lower cost compared to the glass optical fiber sensors [9]. For improving the RI sensitivity, the fiber has been structurally modified by a variety of techniques such as tapering [10–12],side polishing [13–15], making a hole [16–18], etching [19, 20], and coating [21–23].

Polymer optical fiber (POF) modified with in-line submillimeter hole fabricated by micro-drilling directly has been proposed as a compact RI sensor by Shin and Park in which the hole behaves as concave lens. If the hole is filled with a liquid having lower RI than the core, transmittance intensity increases as a function of RI. They reported that decreasing the RI of liquid from 1.5 to 1 leads to a drop in transmission intensity to 65% of its maximum amount [24]. Generally, POF are multi-mode and the sensors fabricated via this optical fiber are classified as intensity modulation schemes. However, wavelength modulation of POF sensors is possible by modifying the sensor via coating. Recently, we have demonstrated a partially unclad type of POF sensor with the ability to detect RI changes in which the cladding diameter is reduced up to ~ 100 nm by etching technique. The maximum sensitivity of ~ 9.1 dB/RIU and ~ 24.2 dB/RIU is achieved for saline and crude oil solution, respectively. There is no shift observed for transmission wavelength [25].

✉ Zahra Samavati
szahra5@graduate.utm.my

✉ Ahmad Fauzi Ismail
afauzi@utm.my

[1] Advanced Membrane Technology Research Centre, Universiti Teknologi Malaysia (UTM), 81310 Johor Bahru, Malaysia

[2] Department of Fundamental and Applied Sciences, Universiti Teknologi Petronas (UTP), 32610 Bandar Seri Iskandar, Malaysia

Bi-layer coating of gold and microposit S1813 film using sputtering method and dip coating technique, respectively, on PMMA polymer optical fiber is proposed by Cennamo et al. to detect the RI changes of the liquid ranges from 1.332 to 1.354 through measuring the wavelength changes [26].

The reported technique for fabrication of partially unclad POF combined with heterostructure deposition of different shape ZnO/Ag film to prepare POF sensors in the current research proposes a novel approach for detecting the crude oil RI gradient at room temperature. Meanwhile, by choosing proper coating configuration, the sensitivity of the optical fiber probe can be improved. Therefore, after fabrication of different POF probes via changing the top layer of nanostructure configuration, the sensors are subjected to a variety of characterization techniques to investigate their structure, morphology, and performance.

2 Experimental

2.1 Materials

The hydrofluoric acid 49%, silver nitrate 98%, ammonia solution 25%, zinc nitrate hexahydrate 98%, sodium hydroxide 98%, tin(II) chloride 98%, palladium(II) chloride 99%, boron hydride dimethylamine 98%, hydrochloric acid 37%, Zinc acetate dihydrate 98%, triethylamine 99.5%, isopropyl alcohol 99.5%, and hexamethylenetetramine 99.0% manufactured by Sigma-Aldrich are used without any further impurity. Malaysia, Miri crude oil with lightness of 43–45° API and sulfur content of 0.04% are used. Multimode POF having core and cladding diameter of 486 µm and 14 µm, respectively, purchased from Jiangxi Daishing POF company is used. The cladding material is fluorinated polymethyl methacrylate (PMMA) with RI of 1.402, and the core is made of PMMA with RI of 1.492. Glass slides with dimension size of 10 mm × 10 mm are used as substrate for PL and UV–VIS/NIR transmission analysis. Glass substrate is employed here because the optical behavior of outer layer which is investigated in this paper is not affected by the substrate and its probable minor effect is deniable.

2.2 Cladding treatment

2.2.1 Removing process

According to the penetration depth of the propagating light, majority of cladding part needs to be removed to boost the sensitivity of the probe. However, removing process should not cause damage along the core/cladding interface and disturb a total internal reflection of light through the fiber. Therefore, online monitoring record on transmission intensity is carried out during the removing process via etching in 40/60 acetone/methanol solution. This mechanism is extensively explained in our earlier research [25].

2.3 Discontinuous Ag nanoparticles coating

The Ag nanoparticles as an inner layer is discontinuously deposited on partially removed cladding polymer optical fiber (Ag/POF) by electroless technique. The partially removed cladding area of the fiber is immersed into 20 ml, 0.1 mol/l $AgNO_3$ solution. Then, Ag is converted to Ag_2O to activate the surface by adding 15 drops of 0.2 mol/l NaOH into the solution. After that, 2 mol/l of ammonia is added slowly to the solution and the glassware is shaken until the precipitate is dissolved totally. At last, 10% concentration glucose solution is added and kept in the 70 °C water bath glassware for 15 min. For discontinuous Ag coating, the fiber should not be kept in the final coating solution more than 15 min; therefore, before this time, probe is taken out from solution and is further proceeded for washing and drying.

2.4 ZnO nanoparticles and nanorods coating

The Ag/POF samples are now subjected for deposition of three different ZnO nanostructures including nanoparticles and horizontally and vertically oriented nanorods as an outer layer (sensing layer) using electroless method. Before ZnO deposition processes begin, the inner layer for all samples need to be activated. Activation process is explained as follows: the Ag-coated part is dipped in aqueous sensitization solutions of 40 g/l $SnCl_2$ and 20 ml/l HCl (37% vol.) for 30 min. Then samples are rinsed in distilled water and after that immersed in 0.1 g/l $PdCl_2$ and 20 ml/l HCl (37% vol.) as an activation solution at room temperature for 30 min. The activated layer is formed homogeneously when the above two steps are repeated for three times. This sample is then ready for final step which is the deposition of different ZnO nanostructures one at a time.

The heterostructure sensing probe is fabricated by coating the ZnO nanoparticles on top of the prepared Ag/POF as follows: (i) 2.28 g of zinc nitrate hexahydrate is dissolved in 75 ml of deionized water at constant temperature of 70 °C. (ii) 0.6 g of NaOH in 150 ml of deionized water is added to solution, dropwise under magnetic stirring for 30 min and then the final solution is cooled down. (iii) In order to coat the fiber with ZnO nanoparticles, fibers are immersed into the above aqueous deposition solution at 70 °C for 3 h without any stirring. (iv) After rinsing in distilled water and drying under the ambient atmosphere, the probe ZnO(nanoparticles)/Ag/POF which is called as sample N is ready for analysis and testing.

The horizontally oriented ZnO nanorods are deposited on the top of the Ag/POF to fabricate second sample as

follows: (i) Solving 0.6 g of zinc nitrate in 100 ml water and stirring for 30 min. (ii) Solving 0.16 g of NaOH in 150 ml of deionized water. (iii) Adding the solution ii to i under stirring until pH of mix solution reaches to 8.3. (iv) Heating the mix solution in micro-oven for 10 min. (v) Cooling at room temperature and centrifuging at 4000 rpm for 10 min. (vi) Rinsing in distilled water and finally, (vii) Immersing the fibers probe part into the above-prepared aqueous deposition solution which contain the ZnO nanorods under ambient temperature of 70 °C for 3 h without any stirring. (viii) Washing and drying the fiber probe. Consequently, bi-layer-coated ZnO(horizontally oriented nanorods)/Ag/POF is completed and the sample name is H.

Coating the vertically aligned ZnO nanorods on Ag/POF includes three steps: preparation of seed solution, preparation of growth solution, and growth of nanorods on fiber surface. For seed solution synthesis, the following steps are followed: (i) 100 mM solution of zinc acetate dehydrate is prepared in 50.0 ml of isopropyl alcohol and then stirred vigorously at 70 °C for 15 min. (ii) 700 µl of 5.0 mmol triethylamine is added and stirred at 70 °C for another 10 min. (iii) this seed solution is cooled to room temperature and protected without stirring for 3 h. For growth solution synthesis, (i) the amount of 7.71 g hexamethylenetetramine is dissolved in 550 ml of DI water. At the same time, 16.4 g of zinc nitrate hexahydrate is dissolved in 500 ml of DI water separately. These two solutions are mixed and stirred for 24 h at room temperature. For nanorods growing on the surface of prepared probe, the Ag/POF sample is dip coated in seed solution for 2 h and then dried at 70 °C. The sample is suspended in growth solution placed in oven at 70 °C for 3 h. The sample is cooled down to room temperature, thoroughly rinsed with DI water, and allowed to air dry. The fabricated sample configuration is ZnO(vertically oriented nanorods)/Ag/POF which is called sample V.

2.5 Experimental setup and characterization of fiber probe

A schematic diagram of the experimental setup is shown in Fig. 1. As shown in the figure, the light source is launched into one of the input ports, and optical spectral analyzer is used to detect the light signals at the output ends. The crude oil–hexane solutions with different volume concentrations (different RI) are prepared as the measurand liquids. The RI of the solutions are measured by an Abbe refractometer and labeled by the equation $n = 1.377 + 0.001C$, where C is the volume concentration of the crude oil at room temperature.

The growth morphology and structure of the probes are characterized using field emission scanning electron microscope (FESEM, JEOLJSM 6380LA) attached with an energy dispersive X-ray spectrometer (EDX), AFM (SPI3800) built by Seiko Instrument Inc.(SII), and XRD (BrukerD8Advance Diffractometer) using Cu-Kα_1 radiations (1.540 Å) at 40 kV and 100 mA. The scanning range of 2θ is from 20° to 80°. For achieving high-quality cross-section FESEM of probe, the sample is preferably dipped into liquid nitrogen, frozen before breaking, and then cut or directly bent and broken. The optical behavior of samples including photoluminescence, absorption, and transmission are studied by room temperature photoluminescence (PerkinElmerLs 55 Luminescence Spectrometer) using a xenon flash lamp under 332 nm excitation wavelength and LAMBDA 1050 UV–VIS/NIR spectrophotometers. A Thorlabs' Stabilized Light Source having the wavelength ranging from 360 to 2600 nm is used as a light source. An optical spectrum analyzer (OSA) (Yokogawa AQ6374) is employed as a light detector. Furthermore, it is used to measure the absorption of crude oil–hexane solutions which is carried out using the quartz cuvette holder with two matched empty cuvettes (i.e., filled with air) for 100% transmittance as a zero/baseline correction for all scans.

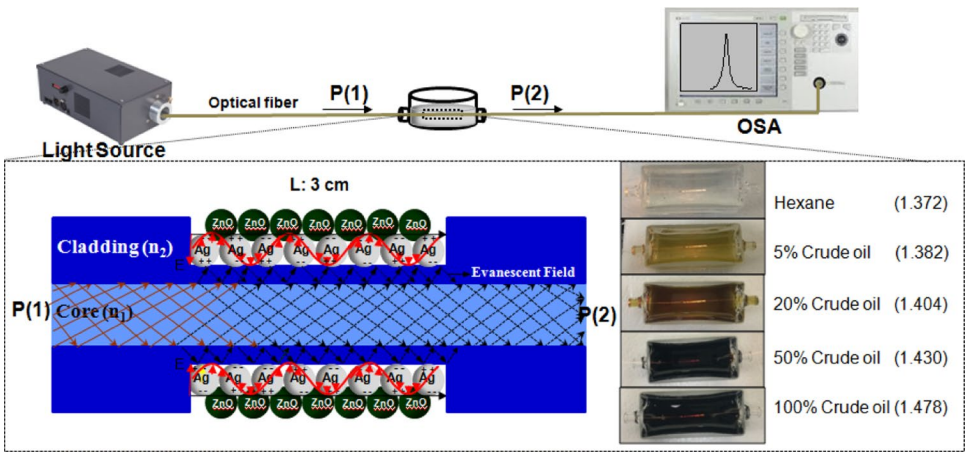

Fig. 1 Schematic representation of the crude oil concentration sensing element formed by ZnO/Ag bi-layer deposition. Real image of immersed fiber probes in crude oil solutions having different concentrations is depicted in the figure

3 Results and discussion

The morphology and bi-layer formation of Ag/ZnO having different top layer configuration deposited on POF is investigated using FESEM and both top view and cross-section images are depicted in Fig. 2. It can be observed that the ZnO top layer includes spherical shape nanoparticles (3c), horizontally aligned nanorods (3f), and vertically oriented nanorods configuration (3i). Ag as a first layer-coated material has ~ 20 nm thickness which is clearly shown in Fig. 2a. The thickness of ZnO-deposited layer consistent of nanoparticles and that of horizontally and vertically oriented nanorods are ~ 150 nm, ~ 100 nm, and ~ 680 nm , respectively. To check the formation and purity of ZnO/Ag/POF, the EDX analysis is employed and the spectra for selected area are depicted in Fig. 2c, f, i. The presence of Zn, O, and Ag confirms the formation of bi-layer on top of POF. The existence of carbon (C) signal is referred to double-side type used for attaching the sample to the holder. The EDX spectra are conducted for selected area in top view of the sample; therefore, missing the strong carbon signal confirm the homogeneous and full distribution of element on top of POF. The analyzing particle tool (ImageJ) software is employed to measure the size distribution of the samples and the results are shown in bar chart in Fig. 3. The particle size is in the range ~from 30 to ~ 60 nm, the average width (height) of horizontally and vertically aligned nanorods are ~ 70 nm(~ 575 nm) and ~ 88 nm(~ 695 nm), respectively.

Figure 4 illustrates the typical X-ray diffraction patterns of the ZnO nanoparticles and vertically and horizontally oriented ZnO nanorods deposited via electroless deposition technique on top of thin Ag/PMMA substrate. The diffraction peaks at $2\theta = 31.9°$, 34.6°, 36.4°, 47.6°, 56.7°, 62.9°, 67.7°, 69.2°, and 75.7°corresponding to the (100), (002), (101), (102), (110), (112), (201), and (202) crystallographic planes of the ZnO hexagonal wurtzite structure are detected in the X-ray diffraction pattern that matches with JCPDS 36-1451 [27]. Intensity of the peaks is proportional to the number of scatters per unit area of a given atomic plane and usually, with increasing plane indices, the intensity of the

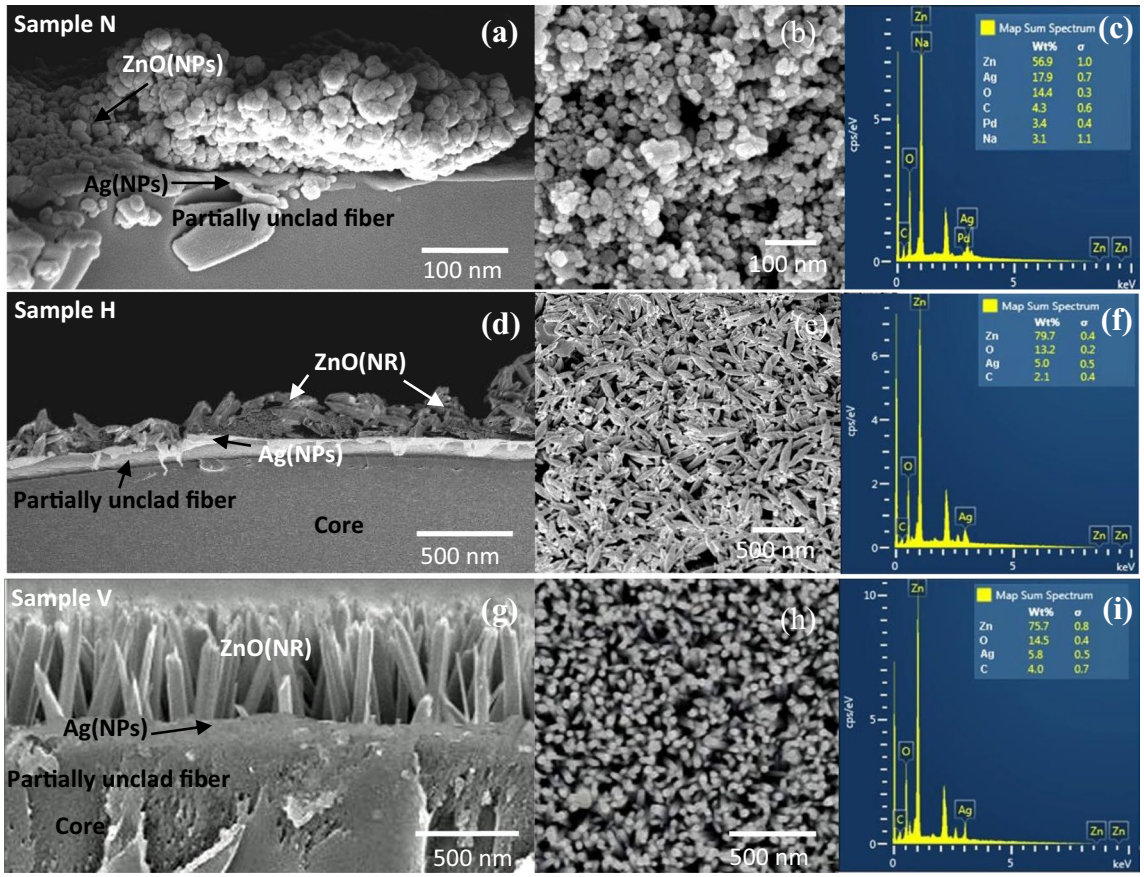

Fig. 2 Cross-sectional FESEM image of deposited ZnO **a** nanoparticles, **d** horizontally oriented nanorods, and **g** vertically oriented nanorods on Ag/POF. Corresponding FESEM surface view EDX spectra for **b**, **c** nanoparticles, **e**, **f** horizontally oriented nanorods, and **h**, **i** vertically oriented nanorods

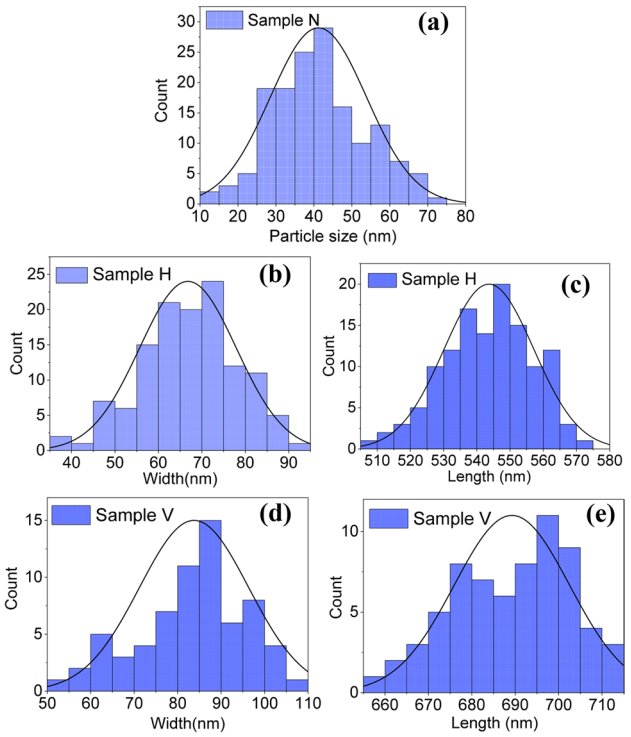

Fig. 3 The histogram of size distribution for ZnO **a** nanoparticles, **b**, **c** horizontally oriented nanorods, and **d**, **e** vertically oriented nanorods

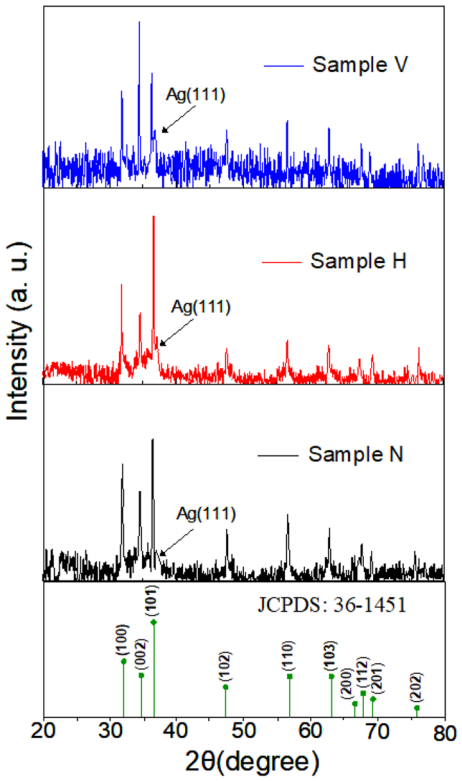

Fig. 4 X-ray diffraction spectra of ZnO nanostructures coated on Ag/PMMA polymer substrate via electroless method

peak decreases as depicted in XRD patterns of all samples. The diffraction and reflection of X-ray occurred through crystallites in polycrystalline materials; therefore, wide peaks with less intensity is expected for nano size structure material compared to bulk counterpart. The size of crystallite is decreased from nanorods (sample V) to nanoparticles (sample N); thus, the intensity of reflected light and as a result the peak intensity diminishes which is depicted in Fig. 4. The crystallite size is inversely proportional to the FWHM of the diffraction peak (Scherer's formula), hence small crystallites generally produces broader peaks. The appearance of intense (002) peak for sample V confirms that the ZnO nanorods are highly crystalline with a hexagonal structure and their preferential orientation growth is perpendicular to the substrate, which is previously observed by the FESEM images as shown in Fig. 2. The c-axis aligned preferred orientation of poly-crystals sample V along their longitudinal axis confirms vertically oriented formation of ZnO nanorods via higher intensity of (002) plane compare to the others. However, in the case of sample H, the intensity of (101) plane is higher showing different alignment of the ZnO nanorods. For all samples, the weak signal of Ag (111) appeared at $2\theta = 38.19°$ which is ascribed to Ag nanofilm coated as an inner layer.

Figure 5 shows representative 3D AFM images of samples which clearly indicate the existence of spherical nanoparticles in sample N and vertical oriented ZnO nanorods in sample V. The deposition of the horizontal aligned nanorods is difficult to define solely from the AFM measurement. The average diameter and length of the ZnO nanorods produced vertically is determined to be ~ 82 nm and ~ 648 nm, respectively. The surface roughness of ZnO nanoparticles and horizontal and vertical nanorods are found to be ~ 32 nm, ~ 276 nm, and ~ 346 nm, respectively. Theoretically, the surface roughness alters the surface area and improves the mechanical interlocking mechanism. The surface roughness affects the filler matrix interfacial bonding and surface energy matching. It is favorable for wetting of the filler and the surface matrix which is required for good adhesion. When the surface of the sample has higher roughness, the possibility of mechanical interlocking formation of crude oil is high; consequently, great adhesion can be realized. Therefore, the higher roughness presented in sample V can assist occurrence of higher level of interaction with crude oil and improve the performance of the sensor.

The optical properties of samples exposed to different crude oil concentrations are studied by room temperature photoluminescence (PL) excited with 332 nm wavelength over a wavelength range of 332–600 nm and the spectra is depicted in Fig. 6. Typical PL spectra of ZnO crystal contains of UV and visible emission peaks where the former is attributed to near band edge (NBE) emission of exciton recombination and the latter is related to deep-level (DL)

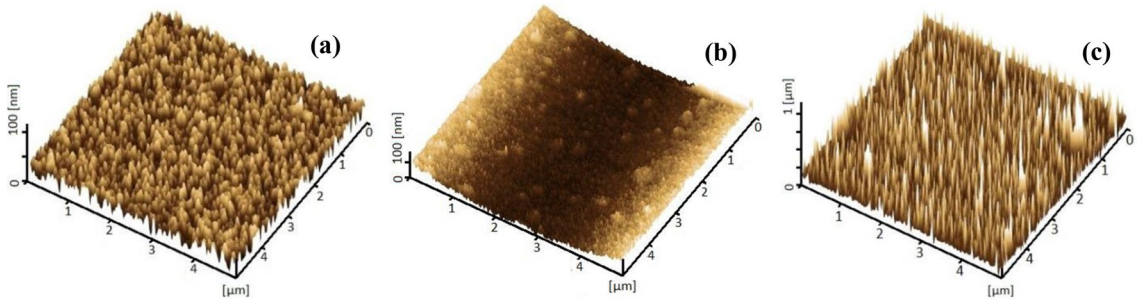

Fig. 5 AFM surface images (5 μm × 5 μm) of **a** ZnO nanoparticles, **b** ZnO horizontally aligned nanorods, and **c** ZnO vertically aligned nanorods deposited on Ag/POF

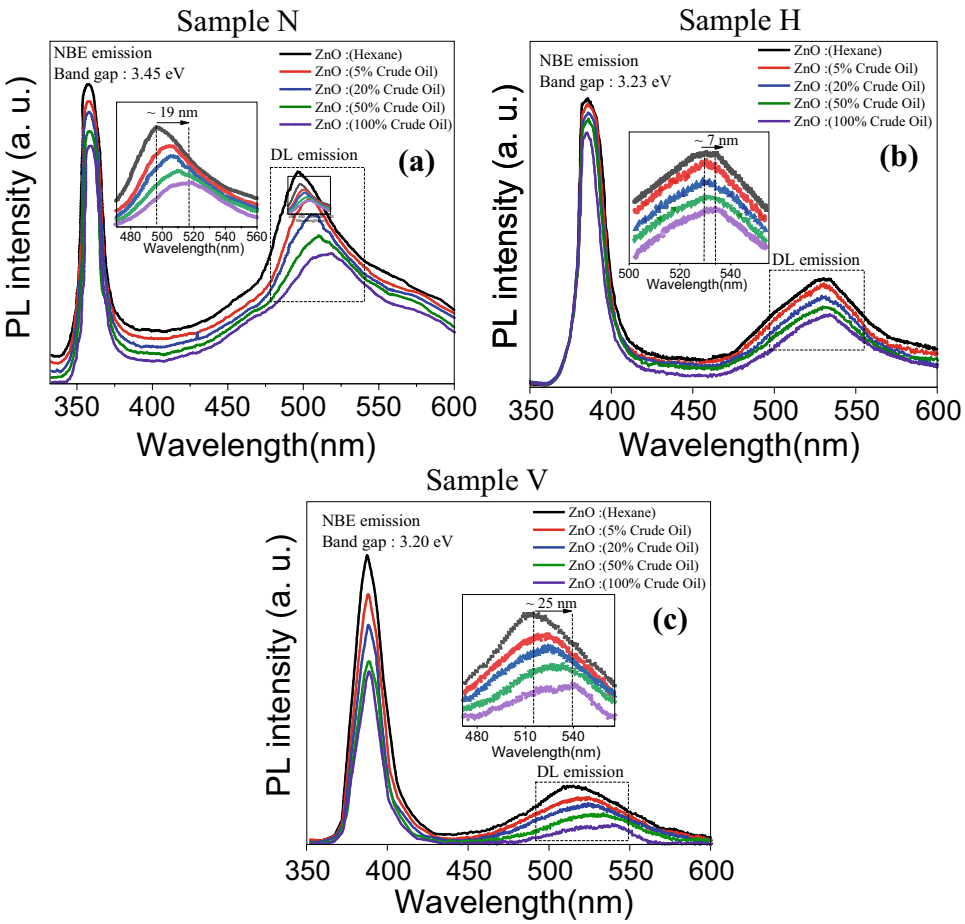

Fig. 6 Photoluminescence spectra of **a** ZnO nanoparticles, **b** horizontally aligned nanorods, and **c** ZnO vertically aligned nanorods deposited on Ag/polymer substrate at room temperature. The excitation wavelength is 332 nm. Inset shows high magnification of DL emission and its corresponding shift due to increasing crude oil concentration

structure defects such as oxygen vacancies (Ov) interstitials (Oi), zinc vacancies (VZn), and interstitials (ZnOi). A strong UV emission and a relatively broad weak shoulder at visible emission are obviously observed for all samples. There are two kinds of shifts that appear in the PL spectra which are explained below.

First, there is a shift in the NBE peak going from sample N to sample V (there is no shift observed in this region by varying the oil concentration in specific sample). The UV emission for three types of ZnO nanostructures illustrates that in the conversion from ZnO nanoparticles to vertically coated ZnO nanorods the signal is ~ 0.25 eV blue shifted. This phenomena is attributed firstly to the residual stress caused by structural imperfections in the ZnO crystals at different morphologies that consequences the band gap modulation and secondly, band gap decreases with increase in size of nanostructure because of electron confinement at nanoscale due to quantum confinement effect. The energy gap

between the highest occupied molecular orbital (HOMO) and the lowest unoccupied molecular orbital (LOMO) for a nanocrystal is significantly modified by distribution of the orbital energies (density of state) in different shape nanostructures. Depending on the geometry and size of the unit cell and atomic structure, the energy wave vector for crystal extends over multiple Brillouin zones; therefore, a large number of energy bands are formed and consequently this orbital splitting restructured the density of energy states resulting in altering of band gap [28]. Accordingly, narrower range band gap energy is anticipated by miniaturization of nanostructures.

Second, there is a shift in the DL emission which is varied by sample shape and crude oil concentration. The blue shift of ~ 0.029 eV, ~ 0.095 eV, and ~ 0.114 eV in deep-level emission at visible area occurred for sample H, N, and V , respectively, by increasing the crude oil concentration from 0 to 100%. The origin of this shift is attributed to electron transferring to the deep energy level of the ZnO. There are six possible bondings between organic and/or inorganic solution and ZnO host surfaces which are mentioned below: covalent connection by anchoring groups, ion exchange/ion pairing or donor/acceptor electrostatic interactions, hydrogen bonding, van der Waals and London forces, hydrophobic interactions resulting in self-assembly of long alkyl chains, and physical trapping inside the pores or cavities of hosts [29]. The ZnO (host surface) interacts with crude oil (organic solution) via two mechanisms of hydrophobic attachment and London force. When the oil touches the ZnO, the weak intermolecular London force is created between temporary dipole crude oil molecules induced by permanent dipole ZnO with wurtzite structure. The charge of the ion causes a distortion of the electron cloud in the non-polar molecule; this constant motion of electrons transfers to a higher orbital. Electrons stay over the forbidden energy gap, into the conduction band, or near the top of the band gap, when the excited state is an anti-bonding orbital. Moreover, the asphaltene and long chain of alkane are available in heavy crude oil. The attraction between ZnO nanoparticles and *n*-C7 asphaltenes has taken place [30]. However, the nanoparticles evaluated also must have the ability to reduce the mean size of asphaltene aggregates in the fluid with the objective of impacting the configuration and distribution of them in the oil matrix. The mean size of the aggregated asphaltene is reduced by ZnO nanoparticles through re-configuration and re-distribution of them in the oil matrix leading to reduction in the crude oil viscosity. Therefore, in diluted environment, the electron can escape from their mutual traction more freely and greater number of them can easily move and occupy the ZnO top energy level. Re-configuration of ZnO energy band structure by electron transferring via above-explained phenomena can modulate the band gap of ZnO when it is exposed to different crude oil concentrations.

The DL-PL shift for sample V is higher due to its larger surface area and open porous structure compare to agglomerated ZnO in sample N and H. Moreover, the average dispersion relation (kinetic energy) of vertically oriented nanorods with more degree of freedom having no periodicity in any direction are higher when compared to compare to horizontally oriented and nanoparticles according to dimensionality of the nanostructures. Therefore, more adsorption of oil molecules even at room temperature and better interaction with crude oil molecules takes place with such a great surface energy. This exclusive property is ascribed to the small size of nanorods and is a key factor for higher sensing performance of the sample V. The PL spectrum of ZnO nanoparticles displays intense visible emissions compared to nanorods samples which is due to enhanced structural defects existing in smaller nanostructure. As it is clearly seen in Fig. 6, lower visible deep-level emission from vertically coated ZnO nanorods compared to UV near band edge emissions represents formation of high-quality ZnO nanorods with lower deep-level defect concentrations. The high UV-to-Visible emission ratio for nanorods confirms a higher level of crystallinity with lower density of surface defects compared to nanoparticles. This statement is consistent with the XRD results presented in Fig. 4.

In order to better understand the sensing behavior of the probes, the optical transmission spectra of Ag/glass, ZnO(nanoparticles)/Ag/glass, ZnO(horizontal nanorods)/Ag/glass, and ZnO(vertical nanorods)/Ag/glass are measured using double-beam spectrophotometer in the wavelength range from 380 to 1800 nm and the spectra shown in Fig. 7. In total internal reflection of propagating light at the core/cladding interface, the light is not reflected completely and a portion of it (evanescent wave) penetrates the cladding and outer layers as well. The evanescent wave intensity exponentially decays as a function of interface distance. This evanescent wave plays a significant role in sensing mechanism. The shape of coated ZnO layer directly affects on

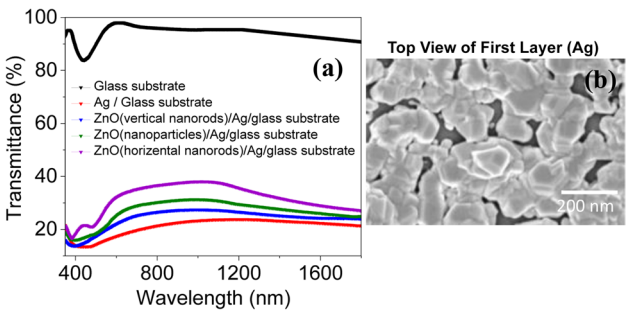

Fig. 7 Optical transmittance spectra of **a** glass substrate, Ag/glass, ZnO (nanoparticles)Ag/glass, ZnO (horizontal nanorods)Ag/glass, and ZnO (vertical nanorods) Ag/glass. **b** Top view FESEM image of Ag coated on partially unclad PMMA polymer fiber. Discontinuous deposition of Ag is clearly seen in the figure

the average transmittance values and it is below 40% for all samples. The Ag/glass (first layer of the probe) exhibits the minimum transmission. Although, Ag exhibit very high reflection for almost all wavelengths above 350 nm, discontinuous coating of Ag nanoparticles on fiber (see Fig. 7b) provides the semi-transparent layer in which transmission the light through first coated layer might be possible.

The light transmittance is increased by coating the ZnO nanostructure on top of Ag layer as shown in Fig. 7. When the ZnO film is formed on the top of Ag layer, the reflection at the interface between the Ag film and air in the emission wavelength region is decreased [31, 32], resulting in increase ofthe transmittance. In particular, the transmittance of the sample H further increases to 37% at 1150 nm, which is higher than that of the other ZnO shape samples. The following equation (Beer-Lambert) shows the relationship between transmission and layer thickness [33]:

$$T = \frac{I}{I_0} = e^{(-\alpha t)} \tag{1}$$

where I is the transmitted intensity at a particular wavelength, I_0 is the incident light intensity, α is the absorption coefficient, and t is the film thickness. The vertical configuration of ZnO sample provides the higher thickness than the horizontally oriented and nanoparticles; therefore, its transmittance is relatively lower. The deposited layer thickness does not directly affect the sensitivity mechanism; however, thickness plays an important role in total internal reflection of the light and contacting evanescent light with outside media. If the deposited layer is too tick, then light cannot contact with outside media and sense the refractive index changes. In contrast, narrow layer leads to occurrence of higher leaky modes and light power lost. Therefore, competition of these two conflict phenomena determine the optimum value for the thickness (~680 for vertically oriented nanorods) in which higher sensitivity and efficiency have taken place.

The wavelength versus absorbance graph of crude oil diluted with different concentrations of hexane is depicted in Fig. 8. In both Vis and IR area, by increasing the oil concentration, the absorption intensity increases. Darker hydrocarbons in higher concentration have less transmittance and, consequently, higher absorption. When the hydrocarbon is exposed to visible light, the absorbed energy of the photon excites the electrons to a higher energy together with occurrence of π–π* transitions. However, when sample is exposed to IR radiation in addition of photon excitation, the following phenomena also occurred. In organic compounds, atoms are bonded through a σ bond and two atoms do not remain static at a fixed distance; thus, their movements are termed stretching and bending vibrations. Both stretching and bending vibrations match with the energies of wavelengths in the

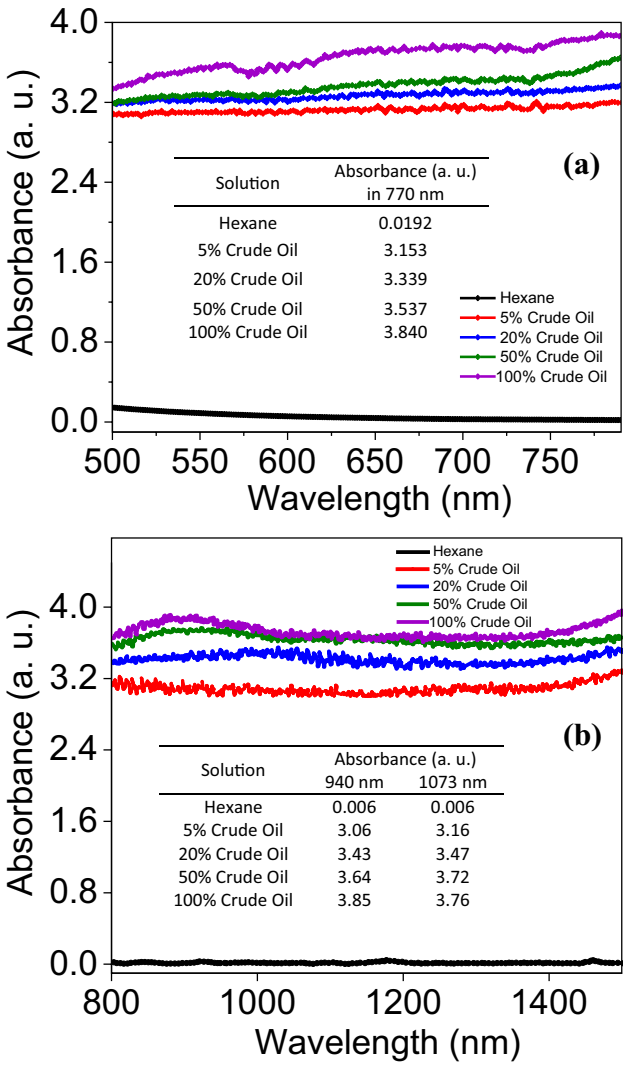

Fig. 8 Room temperature absorbance of crude oil as a function of concentration at **a** visible and **b** IR range. Inset depicts the absorption range in specific selected wavelengths which matches with the main propagating modes through the fiber

infrared region of the electromagnetic spectrum. These two vibrating processes further absorb the part of radiation when the hydrocarbon is exposed to IR light specifically at higher oil concentration. For these reasons, the absorption spectra in IR area is slightly higher than Vis region. This difference is less prominent in lower oil concentration, due to transparency of the solution and lower π–π* transitions.

The light emission spectra range from 550 to 1200 nm which pass through the optical fiber probe displayed in Fig. 9. According to numerical aperture and spectral shape of the source, three peaks appeared in the spectrum corresponding to different propagating main modes. In visible area, the peaks broaden; therefore, for calculating the light feature changes, this area is fitted with Gaussian and shown as inset. Intensity and wavelength modulation are obviously

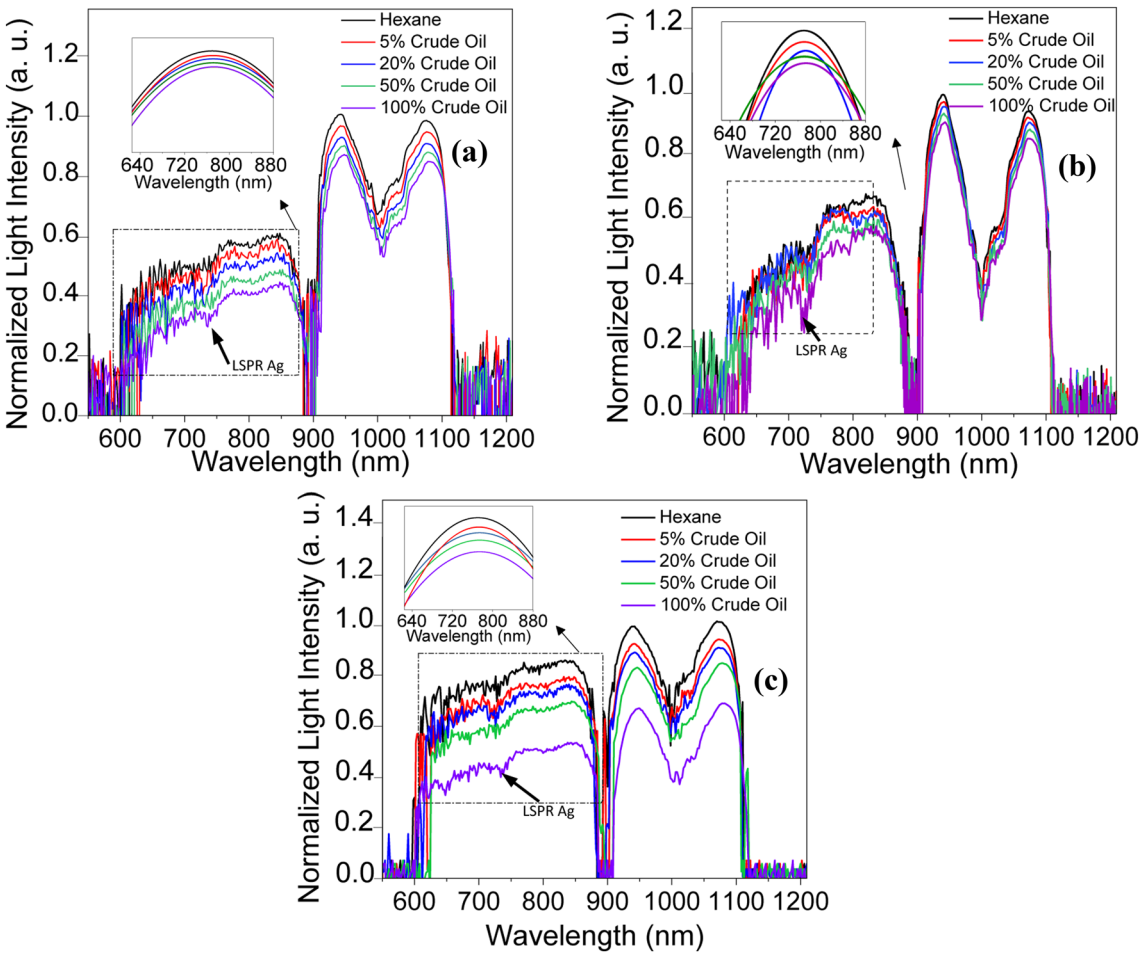

Fig. 9 Transmission spectra of the **a** ZnO(NPs)/Ag/POF, **b** ZnO(NRH)/Ag/POF, and **c** ZnO(NRV)/Ag/POF fiber probe as a function of crude oil concentration. Inset shows Gaussian smoothed propagating mode centered at 770 nm wavelength

seen for all peaks, when the probe immersed in crude oil is having variety of concentrations. However, for the sample V, intensity and wavelength modulation are more prominent compared to the other samples. In visible region of light spectra, there are some small shoulders appearing at 730 nm wavelength. This is associated to localize surface plasmon resonance of coated Ag nanoparticles as a first layer. When Ag NPs are irradiated by evanescent electromagnetic waves in the visible frequency, their surface free electrons start oscillating. This phenomenon enhances the light trapping of propagating light and appears as weak excitonic peaks in the spectra.

Figure 10a and b display the intensity and wavelength changes, respectively, for all samples at three wavelengths matching with main propagating modes. As can be seen in the figures, the intensity and wavelength changes for higher

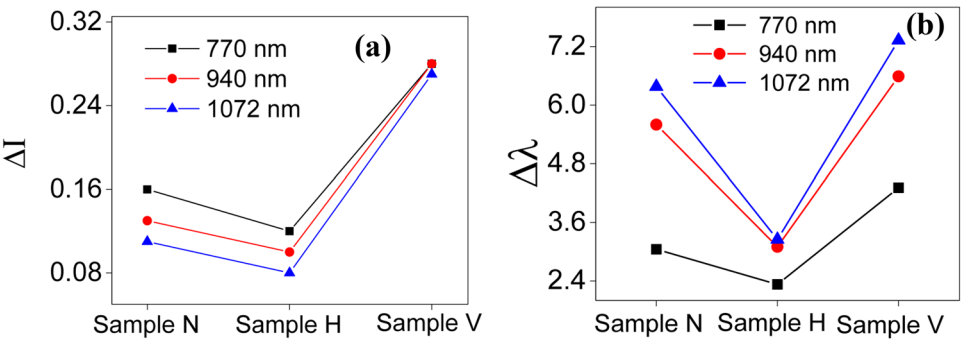

Fig. 10 **a** Intensity and **b** wavelength changes as a function of ZnO shape at propagating mode centered at 770 nm, 940 nm, and 1072 nm wavelength. These three wavelengths are coordinated with the main propagating modes depicted in Fig. 9

wavelength (near IR) are more obvious than visible area which is attributed to deeper penetration of evanescent wave from core to the other layers in this wavelength. Following equation is used to quantitatively calculate the penetration depth [34].

$$d_p = \frac{\lambda}{2\pi n_{\text{core}}\left(\sin^2\theta - \left(\frac{n_{\text{clad}}}{n_{\text{core}}}\right)^2\right)^{1/2}} \quad (2)$$

where the λ is the wavelength of the light source, θ is the incident angle of light, n_1 and n_2 are the RI of core and cladding, respectively. The penetration depth for 770 nm, 940 nm, and 1074 nm wavelength is measured to be 240 nm, 293 nm, and 335 nm, respectively.

The intensity and wavelength modulation of transmitted light as sensing elements for all samples follows the similar trend in which by increasing the oil concentration from 0 to 100% the intensity diminishes and the wavelength is blue shifted. The quantitative value of intensity changes for three different samples while exposed to different crude oil concentration as depicted in Fig. 11a. Increasing the crude oil concentration from 0 to 100% leads to decreasing the intensity to 91%, 86%, and 67% of their maximum value for the samples H, N, and V, respectively. Two phenomena are responsible for intensity modulation: Firstly, interference of core and reflected light from ZnO layer with different RI causes change in intensity, and secondly, evanescence wave absorption dependence on crude oil concentrations. According to Eq. 3 which is experimentally obtained in our previous research [35], when the band gap is altered, the RI of ZnO layer changes.

$$n = A_0\left(1 + Be^{-\text{CE}_g}\right) \quad (3)$$

where n is the RI and E_g is the band gap energy. The parameters of the modified relation are $A = 1.691$, $B = 1.915$, and $C = 0.530\ (\text{eV})^{-1}$. The band gap modification process by exposing to surrounding crude oil is extensively explained in the PL section. When ZnO nanostructures contact the crude oil, by increasing the oil concentration, the electron transfer to ZnO energy bond increases due to higher existence of intermolecular force and inducing electron cloud; therefore, the band gap changes are strongly dependent on oil concentration. Moreover, under the irradiation of incident light having a wavelength larger than the Ag particle size, the high-density electron cloud of the Ag nanoparticles forms and starts oscillating. In case of ZnO/Ag bi-layer configuration at the interface of Ag and ZnO, the electrons accumulate which leads to downward band bending of the ZnO side and transfer of the electrons from Ag nanoparticles to ZnO side. This process correspondingly alters the band gap of ZnO.

The following equation expresses the two-beam optical interference [36]:

$$I = I_1 + I_2 + 2\sqrt{I_1 I_2}\cos\left(\frac{2\pi L\Delta n_{\text{eff}}}{\lambda} + \varphi_0\right) \quad (4)$$

where I is the intensity of the total interference signal detected by optical analyzer, I_1 and I_2 are the intensities of the core and cladding modes,. respectively, L is the length of the prob, λ is the wavelength, and ϕ_0 is the initial phase difference. Cladding mode is propagating the reflected evanescent wave from ZnO layer along the cladding part (see schematic diagram at Fig. 1). Δn_{eff} is the difference between the effective RI of core and cladding modes:

$$\Delta n_{\text{eff}} = n_{\text{eff}}^{\text{core}} - n_{\text{eff}}^{\text{clad}} \quad (5)$$

The max transmission in Eq. 4 appears when $\frac{2\pi L\Delta n_{\text{eff}}}{\lambda} + \varphi_0 = 2m\pi + \varphi_0$ (m is an integer). Consequently, the transmission spectra reveal the peaks at wavelengths given by:

$$\lambda_m = \frac{L\Delta n_{\text{eff}}}{m} \quad (6)$$

The RI of the ZnO layer changes; consequently, the $n_{\text{eff}}^{\text{clad}}$ and Δn_{eff} are altered. The m order interference spectrum shift (λ_m) can be written as follows:

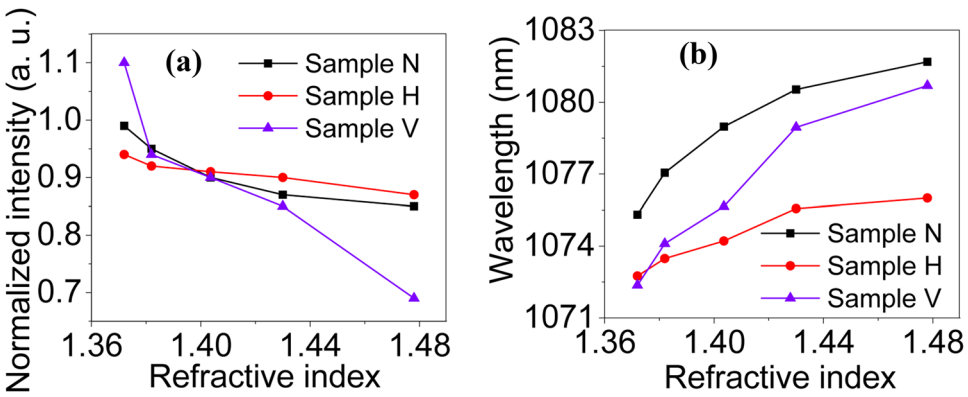

Fig. 11 **a** Intensity and **b** wavelength changes as a function of crude oil RI at propagating mode centered at 1072 nm wavelength for all samples

$$\Delta\lambda_m = \frac{(\Delta n_{\text{eff}} + \Delta n)L}{m} - \frac{\Delta n_{\text{eff}} L}{m} = \frac{\Delta n L}{m} \quad (7)$$

where Δn is the difference between the RI of ZnO and cladding. According to Eq. (7), the shift of the transmission spectra is a function of Δn.

The two parameters of I_2 and $n_{\text{eff}}^{\text{clad}}$ are variable when the probe exposes to different oil concentrations. By increasing the RI of ZnO due to exposure to higher RI of crude oil, the $n_{\text{eff}}^{\text{clad}}$ decreases and as a result, according to Eq. 5, Δn_{eff} increases, and therefore, intensity shrinks. At higher oil concentration as can be seen in schematic diagram (Fig. 1), the color of solution is darker and it is known that light absorption increases by increasing the darkness; accordingly, the absorption of evanescence light which is responsible for core mode propagating is more in dense crude oil.

Figure 11b shows the wavelength shift for samples once the probe is immersed at different oil concentrations. The maximum shift of ~ 3.2 nm, ~ 6.3 nm, and ~ 8.3 nm is observed for sample H, N, and V, respectively, by increasing the RI of crude oil solution from 1.372 to 1.478. The interference of core and cladding mode is responsible for occurrence of wavelength shift. As can be seen in Eq. 7, Δn_{eff} varies when the RI of the reflectance layer (ZnO) changes.

The proposed sensor sensitivity towards crude oil refractive index is compared with the available literature on refractive index polymer fiber optic sensor and the results are presented in Table 1. The table shows that the sensor based on coating the vertically aligned ZnO nanorods (sample V) at higher wavelength light source shows maximum intensity and wavelength sensitivity of 78 nm/RIU and 38 dB/RIU, respectively. The performance of sample V is not only higher than the other proposed samples, but also is greater than the other fabricated POF sensors reported elsewhere. This greater performance is attributed to larger surface area, higher average dispersion relation, better crystallinity, larger surface roughness, better adhesion, and interaction with oil molecules (see schematic in Fig. 12) when the ZnO nanorods are oriented vertically.

4 Conclusion

POF sensors are fabricated and modified by partially removing the cladding and depositing the ZnO/Ag with different ZnO shapes including nanoparticles and horizontal and vertical nanorods on removed region via electroless chemical deposition techniques. The maximum surface area, rms roughness, and crystallinity were obtained for vertically oriented ZnO nanorods sample. Increasing the crude oil concentration modifies the RI of ZnO layer and consequently

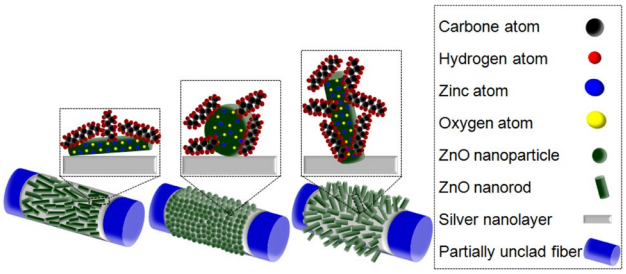

Fig. 12 Schematic diagram of ZnO shape dependence surface interaction with crude oil molecules in the solution

Table 1 Sensitivity comparison of the proposed polymer optical fiber sensor with the recently published one

No	Fiber type	Sensing application based on refractive index changes	Light wavelength (nm)	Sensitivity		Refs.
				Wavelength (nm/RIU)	Intensity (dB/RIU)	
1	POF	Glycerol, dodecane and water	670	–	13.4	[24]
2	POF	Milk fat solutions	530	–	0.15 ΔA/Δ% fat	[37]
3	POF	Sucrose solutions	633	–	29.7	[38]
4	POF	Water content in oil	632		2.21	[39]
5	POF	Sucrose solutions	835	32	–	[40]
6	POF (sample N)	Crude oil solutions	770	28.7	16.9	Current study
			940	52.8	13.2	
			1072	60.1	13.2	
	POF (sample H)		770	21.9	9.4	
			940	29.2	8.5	
			1072	30.6	6.6	
	POF (sample V)		770	40.6	32.0	
			940	62.1	31.1	
			1072	78.5	38.6	

changes the wavelength of propagating light. The highest wavelength sensitivity of 78.5 nm/RIU and intensity sensitivity of 38.6 dB/RIU are obtained for vertically oriented ZnO nanorods sample compared to the other ZnO nanostructure configurations. The utilization of a highly sensitive, flexible, low cost, non-brittle, stress withstanding, and small size intrinsic POF sensor based on exterior cladding modifications for detecting the crude oil concentration permits operation at harsh environment with remote sensing operation capability, where bulk extrinsic sensors are not suitable for use.

Acknowledgements The authors gratefully acknowledge Universiti Teknologi Malaysia and Universiti Teknologi Petronas via vote number R.J130000.7609.4C112. The authors would also like to thank Research Management Centre, Universiti Teknologi Malaysia, and Frontier Material Research Alliance for the technical support.

References

1. S.A. Mohamed, D.M. Beshir, A.A. Rabah, J. Pet. Technol. Altern. Fuels **5**, 26 (2014)
2. B. Yang, B. Yang, J. Zhang, Y. Yin, Y. Niu, M. Ding, Sensors **19**, 96 (2019)
3. B.D. Meshram, A.K. Agrawal, S. Adil, S. Ranvir, K.K. Sande, Int. J. Curr. Microbiol. Appl. Sci. **7**, 3305–3324 (2018)
4. B. Yang, J. Zhang, Y. Yin, Y. Niu, M. Ding, Sensors **19**, 96 (2019)
5. Y. Xu, P. Bai, X. Zhou et al., Adv. Opt. Mater. **7**, 1801433 (2019)
6. B. Xu, J. Huang, X. Xu, A. Zhou, L. Ding, ACS Appl. Mater. Interfaces **11**, 40868 (2019)
7. C.-C. Huang, T.-C. Sun, Sci. Rep. **9**, 1 (2019)
8. J.T. Kim, J. Song, H. Ryu, C.S. Ah, Adv. Opt. Mater. (2019). https://doi.org/10.1002/adom.201901464
9. F. Sequeira, N. Cennamo, A. Rudnitskaya, R. Nogueira, L. Zeni, L. Bilro, Sensors **19**, 2476 (2019)
10. Z. Guo, F. Chu, J. Fan et al., Sens. Rev. **39**, 352 (2019)
11. X. Lu, P.J. Thomas, J.O. Hellevang, Sensors **19**, 2876 (2019)
12. M. Zhang, G. Zhu, L. Lu, X. Lou, L. Zhu, Opt. Fiber Technol. **48**, 297–302 (2019)
13. C. Teng, H. Deng, H. Liu, H. Yang, L. Yuan, J. Zheng, S. Deng, Photonics **6**, 40 (2019)
14. N. Jing, J. Zhou, K. Li, Z. Wang, J. Zheng, P. Xue, IEEE Sens. J. **19**, 5665–5669 (2019)
15. J. Yang, C. Guan, Z. Yu, M. Yang, J. Shi, P. Wang, L. Yuan, Sens. Actuators B **305**, 127555 (2020)
16. S. Sebastian, S. Sridhar, P.S. Prasad, S. Asokan, Appl. Opt. **58**, 115–121 (2019)
17. P. Xue, F. Yu, Y. Cao, J. Zheng, IEEE Sens. J. **19**(17), 7434–7439 (2019)
18. N. Luan, H. Han, L. Zhao, J. Liu, J. Yao, Opt. Mater. Exp. **9**, 819–825 (2019)
19. J. Janting, J. Pedersen, R. Inglev, G. Woyessa, K. Nielsen, O. Bang, J. Lightwave Technol. **37**(18), 4469–4479 (2019)
20. T. Ayupova, M. Sypabekova, C. Molardi, A. Bekmurzayeva, M. Shaimerdenova, K. Dukenbayev, D. Tosi, Sensors **19**, 39 (2019)
21. C. Broadway, R. Min, A.G. Leal-Junior, C. Marques, C. Caucheteur, J. Lightwave Technol. **37**, 2605 (2019)
22. A. Rashid, N. Shamsuri, A. Surani, A. Hakim, K. Ismail, Optoelectron. Adv. Materials-Rapid Commun. **13**, 63 (2019)
23. Y. Zhao, Z.-Q. Deng, Q. Wang, Sens. Actuators B **192**, 229 (2014)
24. J.-D. Shin, J. Park, IEEE Photonics Technol. Lett. **25**, 1882 (2013)
25. Z. Samavati, A. Samavati, A.F. Ismail, N. Yahya, M.A. Rahman, M.H.D. Othman, Opt. Laser Technol. **123**, 105896 (2020)
26. N. Cennamo, D. Massarotti, L. Conte, L. Zeni, Sensors **11**, 11752 (2011)
27. M. Goswami, N.C. Adhikary, S. Bhattacharjee, Optik **158**, 1006 (2018)
28. A. Shaheen, M. Ali, W. Othman, N. Tit, Sci. Rep. **9**, 1 (2019)
29. R. Marczak, F. Werner, J.-F. Gnichwitz, A. Hirsch, D.M. Guldi, W. Peukert, J. Phys. Chem. C **113**, 4669 (2009)
30. E.A. Taborda, C.A. Franco, S.H. Lopera, V. Alvarado, F.B. Cortes, Fuel **184**, 222 (2016)
31. L. Nkhaili, M. Elyaagoubi, A. Elmansouri et al., Spectrosc. Lett. **48**, 536 (2015)
32. C.-C. Ting, C.-H. Li, C.-Y. Kuo, C.-C. Hsu, H.-C. Wang, M.-H. Yang, Thin Solid Films **518**, 4156 (2010)
33. L. Jiao, D. Peng, Y. Liu, AIAA J. **56**, 2903 (2018)
34. I. Bunaziv, O.M. Akselsen, J. Frostevarg, A.F. Kaplan, J. Mater. Process. Technol. **256**, 216 (2018)
35. Z. Samavati, A. Samavati, A.F. Ismail, M.H.D. Othman, M.A. Rahman, Opt. Fiber Technol. **52**, 101976 (2019)
36. Q. Wang, Y. Liu, Measurement **130**, 161 (2018)
37. A. Gowri, A.S. Rajamani, B. Ramakrishna, V.V.R. Sai, Opt. Fiber Technol. **47**, 15 (2019)
38. F. De-Jun, L. Guan-Xiu, L. Xi-Lu, J. Ming-Shun, S. Qing-Mei, Appl. Opt. **53**, 2007 (2014)
39. D.K. Mahanta, S. Laskar, IEEE Sens. J. **18**, 1506 (2017)
40. S. Zhang, Y. Guo, T. Cheng, S. Li, J. Li, Optik **212**, 164697 (2020)